

**Electric potential barriers in the magnetic nozzle**Zhiyuan Chen <sup>1</sup>, Yibai Wang,<sup>1</sup> Haibin Tang <sup>2,4,6,\*</sup>, Junxue Ren,<sup>1</sup> Min Li,<sup>5</sup> Zhe Zhang <sup>3</sup>, Shuai Cao,<sup>1</sup> and Jinbin Cao<sup>2,6</sup><sup>1</sup>*School of Astronautics, Beihang University, Beijing 100083, China*<sup>2</sup>*School of Space and Environment, Beihang University, Beijing 100083, China*<sup>3</sup>*School of Instrumentation and Optoelectronic Engineering, Beihang University, Beijing 100083, China*<sup>4</sup>*Key Laboratory of Spacecraft Design Optimization and Dynamic Simulation Technologies of the Ministry of Education, Beihang University, Beijing 100083, China*<sup>5</sup>*Shanghai Engineering Centre for Microsatellites, Chinese Academy of Sciences, Shanghai 201203, China*<sup>6</sup>*Laboratory of Space Environment monitoring and Information Processing, Ministry of Industry and Information Technology, Beijing 100083, China*

(Received 29 June 2019; revised manuscript received 1 April 2020; accepted 28 April 2020; published 26 May 2020)

Magnetic nozzles are convergent-divergent applied magnetic fields which are commonly used in electric propulsion, manufacturing, and material processing industries. This paper studies the previously overlooked physics in confining the thermalized ions injected from a near-uniform inlet in the magnetic nozzle. Through fully kinetic planar-3V particle-in-cell (PIC) modeling and simulation, an electric potential barrier is found on the periphery of the nozzle throat, which serves to confine the thermalized ions by the electric force. With the initial thermal energy as driving force and insufficient magnetic confinement, the ions overshoot the most divergent magnetic line, which results in the accumulation of positive space charges around the throat. The accumulated charges would create an ion-confining potential barrier with limited extent. Apart from the finite-electron Larmor radius (FELR) effect, two more factors are put forward to account for the limited extent of the potential barrier: the depletion of ion thermal energy and the short-circuiting effect. The influences of inlet temperature ratio of ions to electrons and magnetic inductive strength  $B_0$  are quantitatively investigated using the PIC code. The results indicate that the potential barrier serves as a medium to transfer the gas dynamic thrust to the magnetic nozzle while providing constrain to the ions, like the solid wall in a de Laval nozzle. In high- $B_0$  regime, the finite-ion Larmor radius (FILR) effect becomes dominant rather than the FELR effect in the plasma confinement of magnetic nozzles.

DOI: [10.1103/PhysRevE.101.053208](https://doi.org/10.1103/PhysRevE.101.053208)**I. INTRODUCTION**

The magnetic nozzle (MN) is usually a convergent-divergent magnetic field used to guide the plasma flow and transfer the nondirected kinetic energy to the directed one [1]. They are commonly used in electric propulsion [2–5], advanced manufacturing, and material processing [6]. The magnetic nozzle acts functionally like a de Laval nozzle, but incorporates plasma-field interactions to constrain and accelerate the plasma flow, which avoids direct wall-plasma contact that may damage the wall in the long run. Moreover, the shape of the magnetic nozzle can be easily changed to control the thrust vector without using the mechanical gimbals [7–9].

Ever since the concept of magnetic nozzles was put forward, numerous studies have been done to explore the physics in MNs, either by experiments [10–18] or theories and simulations [19–24]. These pioneer studies gained much insights into the physical details of magnetic nozzles and revealed the existence of ambipolar acceleration. In recent years, Arefiev and Breizman developed the rarefaction wave theory [25]

and Sheehan *et al.* presented the adiabatic expansion theory [26] to further explain the ambipolar acceleration. In addition, another acceleration mechanism featuring a potential structure named current-free double layer has been reported to exist in the MN of helicon plasma thrusters (HPTs) [3]. In the last 25 years, research has focused on detachment processes in MNs. Based on different cold MHD models, Moses *et al.* [27], Hooper [28], and Arefiev and Breizman [29] put forward different detachment mechanisms related to resistivity, electron inertia, and induced magnetic field, respectively. The inertia detachment has been studied extensively; some believe the hybrid Larmor radius can be an effective criterion for detachment [28,30,31] while others argue that only electron demagnetization guarantees detachment [32]. About the induced field detachment, Ilin *et al.* [33] and Winglee *et al.* [34] acquired similar conclusions to that of Arefiev and Breizman [29], whereas, the direction of induced current is much debated, and the self-demagnetization detachment has been proposed [35,36]. Recently, the first laboratory observation of the spatial transition of the direction of induced current from diamagnetic to paramagnetic has been done by Takahashi and Ando [13]. Detachment may also be achieved through recombination [37], charge-exchange collisions, and magnetic reconnection.

\*thb@buaa.edu.cn

Most of the theoretical studies on the magnetic nozzle assumed that the ion temperature can be neglected when compared with electron temperature, which is applicable to many plasma sources, such as helicon thrusters and Hall-effect thrusters. And, the lateral confinement is obtained by canceling out the electron pressure by the Lorentz force acting on the azimuthal electron currents near the throat region. Nevertheless, magnetic nozzle of other plasma sources like Variable Specific Impulse Magnetoplasma Rocket (VASIMR) and Magnetoplasmadynamic Thruster (MPDT) cannot comply with this hypothesis. When the ion temperature is considered, it is natural to assume that the electric field is responsible for the ion confinement in the magnetic nozzle where the ions are essentially unmagnetized. However, the detailed structure of the electric field and its properties remain unknown.

Merino *et al.* proposed a model explaining that a radial electric field can be established to counter the ion pressure [38]. This theory explains the nonuniform-inlet case efficiently and the similar convexity distribution of isopotential lines can also be found in Ilin's studies [33]. The area above the maximum divergent magnetic line [MDML, the magnetic line that intersects  $(x, z) = (R_{p0}, 0)$ ] is not included in the simulation domain in both studies, where the plasma parameters are unknown. This area is named as "outer-MDML" area below. Moreover, if the density profile of the inlet is near uniform, the pressure gradient will be concentrated on the inlet edge, which makes the outer-MDML area more significant for the understanding of the lateral confinement in the MN.

Shoucri *et al.* also considered the confinement of thermalized ions when investigating the charge separation near the plasma-wall transition area with a steep density gradient [39,40]. In their work, a one-dimensional Eulerian VLASOV code was used to capture the temporal evolution of the plasma parameters, and an oscillating positive potential bump was discovered toward the edge of the plasma, which is responsible for the confinement of the thermalized ions. In their paper, the pressure force is essentially balanced by the electric field along the density gradient. While their work provided great insights into the physics behind the confinement mechanisms at the edge, there are three major factors which limit its applicability to our research subject. Firstly, the electrons were assumed to be frozen along the magnetic lines; thus, the finite-electron Larmor radius effect was totally neglected, which is significant when the magnetic strength is relatively low. Secondly, the boundary on the outer side is assumed as either a floating cylindrical vessel [40] or a grounded vessel [39], which is quite different from the condition we consider in the study of the magnetic nozzle—a plasma-vacuum boundary. Thirdly, the magnetic topology employed in their model is nearly perpendicular to the radial direction, which also differs from the divergent magnetic topology of the MN.

Some examples can also be found in the literature, which can give some inspiration of the outer-MDML area in the cold-ion cases. According to the experiment conducted by Charles [41] using a helicon plasma source and a simulation study by Singh *et al.* [42], a potential sidelobe is discovered just outside the plasma edge which coincides with the U-shaped double layer in the HPD device. In Little and Choueiri's study [43] on MN, they discovered a potential

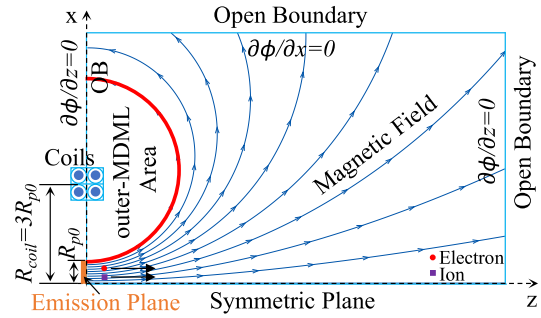


FIG. 1. Computational domain and boundary condition settings. The MDML is represented by the red bold line and the outer-MDML area is indicated on the figure.

well at the downstream periphery of the plasma which can serve as an ion-confining structure. Both studies claim that the potential structures are related to plasma instabilities—the two-stream instability in the former study and ion acoustic turbulence in the latter. However, in neither study was the inlet ion temperature considered.

In some magnetic nozzle applications, inlet ion temperature should be considered; thus, it makes the outer-MDML area more significant for the comprehension of the confinement of the unmagnetized ions, especially in the uniform-inlet case. This paper extends the fully kinetic particle-in-cell code in a previously published study [44] to include both the inlet ion temperature and the outer-MDML area to simulate the plasma flow in the magnetic nozzle and an electric potential structure, named the electric potential barrier, is found beyond the magnetic nozzle throat. In addition, the influence of inlet temperature ratio  $T_{i0} : T_{e0}$  and magnetic inductive strength  $B_0$  on the behaviors of the electric potential barrier is further investigated.

## II. NUMERICAL METHODS AND BOUNDARY CONDITIONS

### A. Overview of the numerical methods

To investigate the influence of ion temperature, the fully kinetic two-dimensional-3V PIC model reported in our previous work [44] was extended to include a warm-ion inlet and the background magnetic field, and then used to simulate the magnetic nozzle with a uniform inlet in this paper.

In this case, the plasma is assumed to be fully ionized and collisionless as the mean-free path is orders of magnitude larger than the size of magnetic nozzle throat. The computational domain along with the boundary settings and the magnetic topology is depicted in Fig 1. The magnetic field is generated by a virtual coil composed of  $4 \times 4$  current loops and the induced magnetic field is neglected since the region we focused on is near the magnetic nozzle throat where the applied field is dominant. Because of the uncertainty of the effects on the magnetic nozzle simulations brought by the numerical acceleration techniques of the PIC-MCC methods, i.e., increasing the vacuum permittivity, reducing the mass of heavy particles, and making use of self-similarity [45–47]. These methods are not incorporated into the code; instead, the simulation domain is shrunken to a few hundred Debye

lengths as Rao and Singh [48] and Li *et al.* [44] did in their work. To do that safely, while the setup of the initial parameters of the simulation, the dimensionless ion cyclone frequency  $\hat{\Omega}_{i0} = \frac{eB_0R}{m_i u_{i0}}$ , brought by Ahedo and Merino [49], is kept the same as the one in a real-scale magnetic nozzle system to keep the degree of ion magnetization constant before and after the scaling. In the expression of  $\hat{\Omega}_{i0}$ ,  $e$  denotes elementary charge,  $B_0$  denotes the magnetic strength at the magnetic nozzle throat,  $R$  denotes the width of plasma inlet,  $m_i$  is the mass of ions, and  $u_{i0}$  is the ion inlet velocity. The reason to keep  $\hat{\Omega}_{i0}$  constant is that the electrons are usually strongly magnetized in the applications of a propulsive magnetic nozzle, while the ions are undermagnetized which facilitates the generation of the electric potential barrier. Therefore, the magnetization degree of ions are more sensitive to  $B_0$  variation and more representative of the physics behind this electric structure. Moreover, the proton is considered as ion to further reduce the computational time.

In the PIC model, ions and electrons are modeled as macroparticles separately. And, macroparticles are moved by solving Newton-Lorentz equations using the standard leapfrog Boris scheme [50,51]. The self-consistent electric field is calculated by solving Poisson equations with the dynamic alternating direction implicit (DADI) method.

As depicted in Fig. 1, the computational domain is a rectangle area, which has the length of 200 cells and a width of 120 cells with a grid resolution of one Debye length  $\lambda_{D0}$  which allows for stable simulations. In addition, simulations were run using a time-step resolution of  $\Delta t \omega_{pe} = 0.1$ .

As for the boundary settings, the lower part of the left boundary stands for the plasma inlet (particle emission plane) with a length of  $R_{p0} = 10\lambda_{D0}$ . The boundary on the bottom is the symmetric plane. Other boundaries (upper left, upper and right) are open boundaries representing the infinite vacuum environment. The central plane of the virtual magnetic coil coincides with the plane represented by the left boundary, and the center of the coil is at the origin, which means the plasma inlet is also the magnetic nozzle throat and the radius of the coil is  $R_{coil} = 3R_{p0}$ .

## B. Boundary conditions

Since the induced magnetic field is neglected, there remain only two kinds of boundary conditions: electric field and particle movements. For the electric-field boundary, the potential of the inlet is set to 0 V as a reference potential. The open boundaries and the symmetric boundary are set as Neumann condition as noted in Fig. 1. The particle motion boundary conditions are much more complicated than those of the electric field.

At each time step, ions and electrons are emitted from the inlet boundary along the  $z$  axis, the density profile is assumed to be uniform, and the Mach number of the inlet plasma is 1.0. Note that the velocity used to calculate the Mach number is ion acoustic velocity  $v_s = (\frac{\gamma_e k_B T_e + \gamma_i k_B T_i}{m_i})^{1/2}$ , where  $\gamma_e = 1$  and  $\gamma_i = 1.667$ . The electrons are sampled from a Maxwellian distribution with a drift component equaling to the ion drifting velocity. Since the ion temperature is not negligible in the current model, and the drift velocity  $v_0$  and the ion thermal velocity  $v_{i0}$  cannot satisfy the condition  $v_0 \gg$

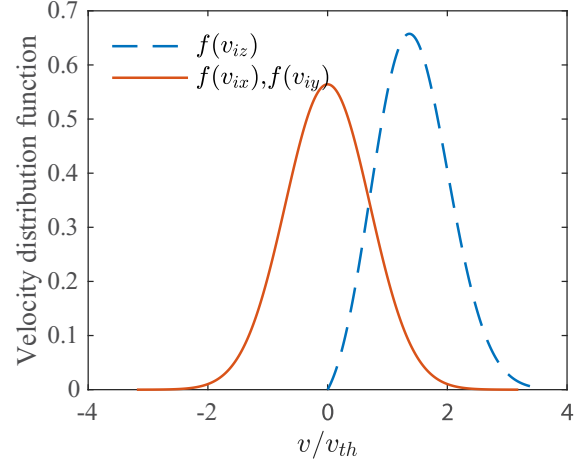


FIG. 2. Velocity distribution function of the emitted ions.

$v_{i0}$  under low Mach number, the ion velocity distribution in the  $z$  direction requires the use of the drifting Maxwellian flux [52], while the other directions still follow a stationary Maxwellian distribution. The velocity distribution functions of electrons and ions are as follows:

$$f_e(v_{ex,ey,ez}) = \sqrt{\frac{m_e}{2\pi k_B T_{e0}}} \exp\left(-\frac{m_e}{2k_B T_{e0}} v_{ex,ey,ez}^2\right), \quad (1)$$

$$f_i(v_{ix,iy}) = \sqrt{\frac{m_i}{2\pi k_B T_{i0}}} \exp\left(-\frac{m_i}{2k_B T_{i0}} v_{ix,iy}^2\right), \quad (2)$$

$$f_i(v_{iz}) = A v_{iz} \exp\left(-\frac{m_i}{2k_B T_{i0}} (v_{iz} - v_0)^2\right). \quad (3)$$

The coefficient  $A$  in Eq. (3) can be obtained through normalization conditions.

$$A^{-1} = \sqrt{\frac{k_B T_i}{2\pi m_i}} \exp\left(-\frac{m v_0^2}{2k_B T_i}\right) + \frac{v_0}{2} \left(\operatorname{erf}\left(v_0 \sqrt{\frac{m_i}{2k_B T_i}}\right) + 1\right). \quad (4)$$

The velocity distribution function of ions is illustrated in Fig. 2.

As stated in our previous work [44,53], we think quasineutrality and current-free condition should both be conserved globally within the plasma source. However, considering the counter streaming of electrons [25], it is difficult to guarantee these two conditions by the setting of the inlet boundary alone, thus they are guaranteed by both the inlet and open boundary settings:

Quasineutrality  $n_{i0} = n_{e0}$  and current-free condition  $\mathbf{J}_{i0} = \mathbf{J}_{e0}$  is forced at the inlet boundary.

At each time step, return those electrons which have relatively lower energy based on the global current-free condition when they cross the open boundaries.

To be more specific, at the inlet boundary, the number of injected electrons are adjusted each time step according to the difference between the local electron density and ion density, and the axial component of electron velocity at the inlet  $v_{ez0}$  should include both the thermal velocity  $v_{ez,t}$  from Eq. (1) and

TABLE I. Simulation parameters in the verification case.

Parameters (unit)	Value
$B_0$ (G)	1000
$R_l/R$	5.4
$n_0$ ( $\text{m}^{-3}$ )	$7 \times 10^{18}$
$T_{e0}$ (eV)	20
$\hat{\Omega}_{i0} \equiv R\Omega_{i0} / c_s$	0.1

a drifting velocity equal to the ions', as given by Eq. (5).

$$v_{ez0} = v_{ez,t} + \overline{v_{iz0}}. \quad (5)$$

At the open boundary, if not specially attended to, the number of escaping electrons will be larger than that of ions because of the higher mobility of the electrons and the escaping electrons are simply deleted. This habitual treatment not only forces the simulation to be stopped before reaching the steady state to prevent border effects and unavoidable instabilities [54,55], but also makes the simulated physical picture inaccurate because of the inability to reproduce the whole procedure of the trapped electrons [56]. As noted in our previous work [44], in order to keep the global current-free condition  $\mathbf{J}_i = \mathbf{J}_e$  at the outer edge, during each time step, the electrons and ions passing the open boundary are recorded. Specifically, these escaping electrons are sorted according to their kinetic energy, then the electron with the lowest energy will be specularly reflected back into the domain; the reflection is carried out repeatedly until the number of escaping free electrons equals to that of escaping ions.

### III. BENCHMARK VERIFICATION

This code was developed based on a PIC-MCC simulation code package which has been successfully applied in the simulations of plasma thruster plume [44], Hall-effect thrusters [57], hollow cathodes [58], and MPD thrusters [59,60].

Before this code can be used to study the magnetic nozzle, it ought to be verified for the sake of accuracy. In the literature, the data of magnetic nozzle with a uniform inlet are limited, so the simulation results of the two-fluid code DIMAGNO are used as a comparison [49]. The plasma parameters at the nozzle inlet and magnetic field settings are presented in Table I. These parameters are based on the experimental data of Batishchev's helicon plasma thruster [61]. The fully ionized argon plasma is selected to conduct the simulation.

The simulation results of our PIC code and DIMAGNO along the axis are compared.

Similar to what was stated in our previous work [44], the choice of a planar geometry instead of a cylindrical one results in the incapacity of expansion in the  $y$  direction (or the  $\theta$  direction in a cylindrical system); therefore, while the plasma expands downstream, the simulated number density and electric potential will decrease slower than that of the DIMAGNO code which used a cylindrical geometry. In order to be able to compare the planar results and cylindrical results directly, we derived a scaling law that can scale our planar results to their equivalents in the cylindrical geometry. The basic principle of the scaling law is to keep the number of

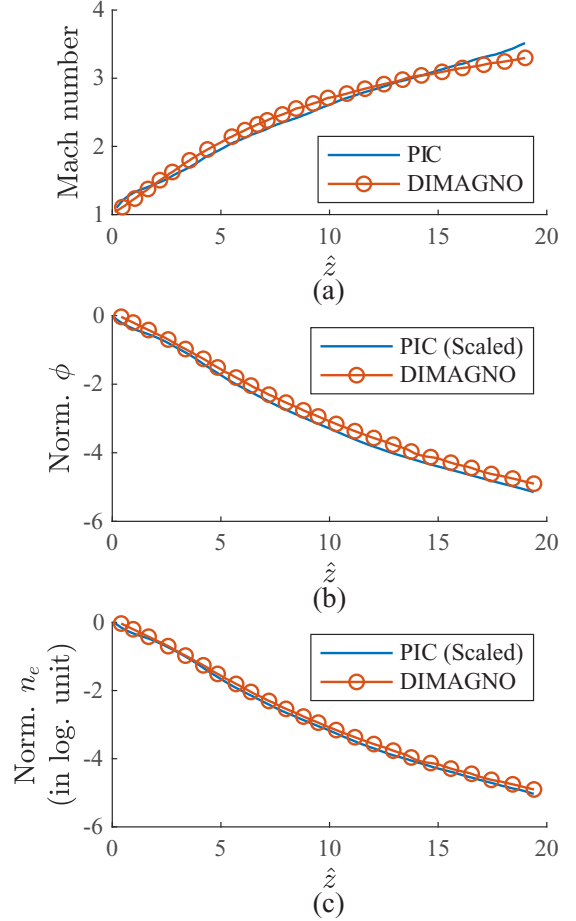


FIG. 3. Comparisons of the simulation results (along  $z$  axis) between PIC code and DIMAGNO code. (a) Comparison of Mach number profile. (b) Comparison of normalized electric potential profile. (c) Comparison of normalized number density.

particles unchanged in the cell, while the volume of the cell is changed from a slat in the planar geometry to a disk in the cylindrical geometry. After derivation (see the Appendix), the scaling laws for the number density and the electric potential along the  $z$  axis are as follows. As for the Mach number, it requires no scaling in that the electron temperature used to compute the ion acoustic velocity is also affected by the incapacity of expansion in the  $y$  direction.

$$\hat{n}_{\text{scaled}}(\hat{z}) = \hat{n}_{\text{planar}}(\hat{z}) \cdot \sqrt{\frac{B(\hat{z})}{B_0}}, \quad (6)$$

$$\hat{\phi}_{\text{scaled}}(\hat{z}) = \hat{\phi}_{\text{planar}}(\hat{z}) + \frac{1}{2} \ln \frac{B(\hat{z})}{B_0}, \quad (7)$$

where  $B(\hat{z})$  and  $B_0$  denote the magnetic strength along the  $z$  axis and at  $\hat{z} = 0$ , respectively,  $\hat{n}_{\text{planar}}$  and  $\hat{\phi}_{\text{planar}}$  are the planar results directly simulated,  $\hat{n}_{\text{scaled}}$  and  $\hat{\phi}_{\text{scaled}}$  are the scaled results used to be compared with the DIMAGNO ones. The comparisons of Mach number, electric potential, and plasma number density are shown, respectively, in Figs. 3(a)–3(c).

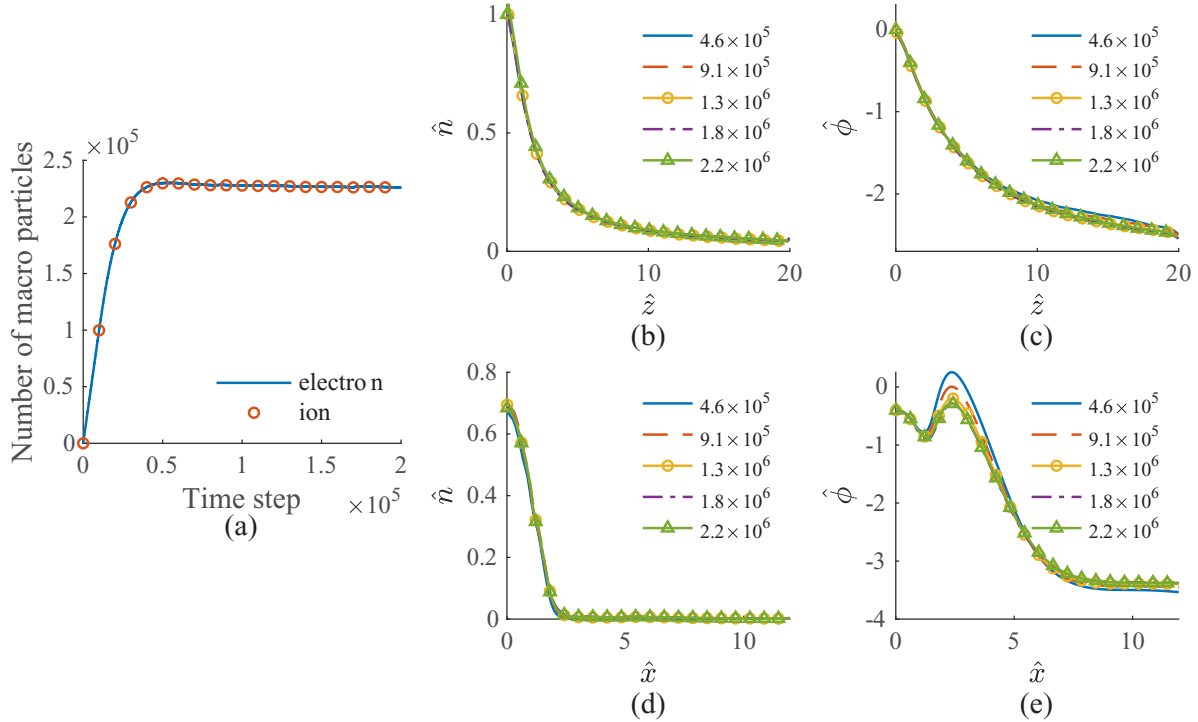


FIG. 4. Convergence study and sensitivity study on the particle number. (a) Number of computed macroparticles versus simulation time. (b), (c) Axial profile ( $\hat{x} = 0$ ) of electron density and electric potential simulated under different particle number. (d), (e) Lateral profile ( $\hat{z} = 1$ ) of electron density and electric potential simulated under different particle number.

As can be seen from Fig 3, the simulation results of Mach number, electric potential, and plasma number density are all in good agreement with the results of DIMAGNO. Therefore, apart from the influence brought by the planar geometry, the PIC code can accurately describe the evolution of plasma in the magnetic nozzle and can be used for further research work.

Note that in the following sections, the proton, rather than the argon ion used by DIMAGNO, will be used as the only species of ion to conduct the research in order to reduce the computational time to a practical level. Despite the usage of disparate ion-to-electron mass ratio, the results of DIMAGNO were still chosen to verify the code due to the fact that the experimental data of MN using hydrogen and similar boundary conditions are either hard to find in the literature or the description is vague. In addition, the effect of ion-to-electron mass ratio has been considered in the above-mentioned scaling law based on  $\hat{\Omega}_{i0}$ , in which  $B_0$  scales with  $m_i/[L]$ . Therefore, the qualitative nature of the results will not change when the code is applied to the research using protons as ions.

## IV. RESULTS AND DISCUSSION

### A. Simulation results and the cause of the electric potential barrier

To investigate the constrain mechanism of the magnetic nozzle on the thermalized ions, two simulation cases with different inlet temperature ratios  $T_{i0} : T_{e0} = 2.4 : 1$  and  $T_{i0} = 0$  are compared.  $T_{i0} + T_{e0} = \text{const}$  is conserved to ensure that the total energy remains the same. The inlet number density and total temperature are set as  $1 \times 10^{18} \text{ m}^{-3}$  and 20 eV,

respectively, referenced from the experimental results of the helicon source of a 24-kW VASIMR in the literature [62]. The inlet magnetic field is 2000 G, under which the magnetic-field characteristic variation length at the inlet is  $L_{\text{cha0}} = 0.1 B_0 / \nabla B \sim R_{p0}$  which is compared with particle Larmor radius later in this paper to determine the magnetization state of ions and electrons. Similar high-Gauss cases can also be found in the experiments [61,63,64]. If not specified otherwise, the results shown in this paper use the following normalization:  $x$ ,  $z$  are normalized by inlet length  $R_{p0}$ , velocities are normalized by electron thermal velocity  $v_{te0}$ , electric potential  $\phi$  and  $T_e$ ,  $T_i$  are normalized by the total temperature at the inlet  $T_{e0} + T_{i0}$ , and number density is normalized by electron number density at the inlet  $n_{e0}$ . The “0” in the subscript indicates inlet parameters.

In a typical simulation case, a total number of  $4.6 \times 10^5$  macroparticles were simulated; the convergence plot based on the numbers of simulated macroparticles is shown in Fig. 4. As can be seen from Fig. 4(a), the simulation reached the stable state in less than  $10^5$  time steps (i.e.,  $10^4 \omega_{pe}^{-1}$ ); the macroparticle numbers of electrons and ions are so close that it is hard to distinguish one from the other. In addition, a series of sensitivity studies on the number of macroparticles are conducted in order to exclude the possibility that this electric potential barrier might originate from the numerical diffusion. The axial profiles are shown in Figs. 4(b) and 4(c), where it can be seen that the simulated axial profiles of normalized electron density and electric potential are nearly unchanged when the total number of simulated particles rises from  $4.6 \times 10^5$  to  $2.2 \times 10^6$ , while in the lateral direction, the profiles of number density are almost independent of the particle number

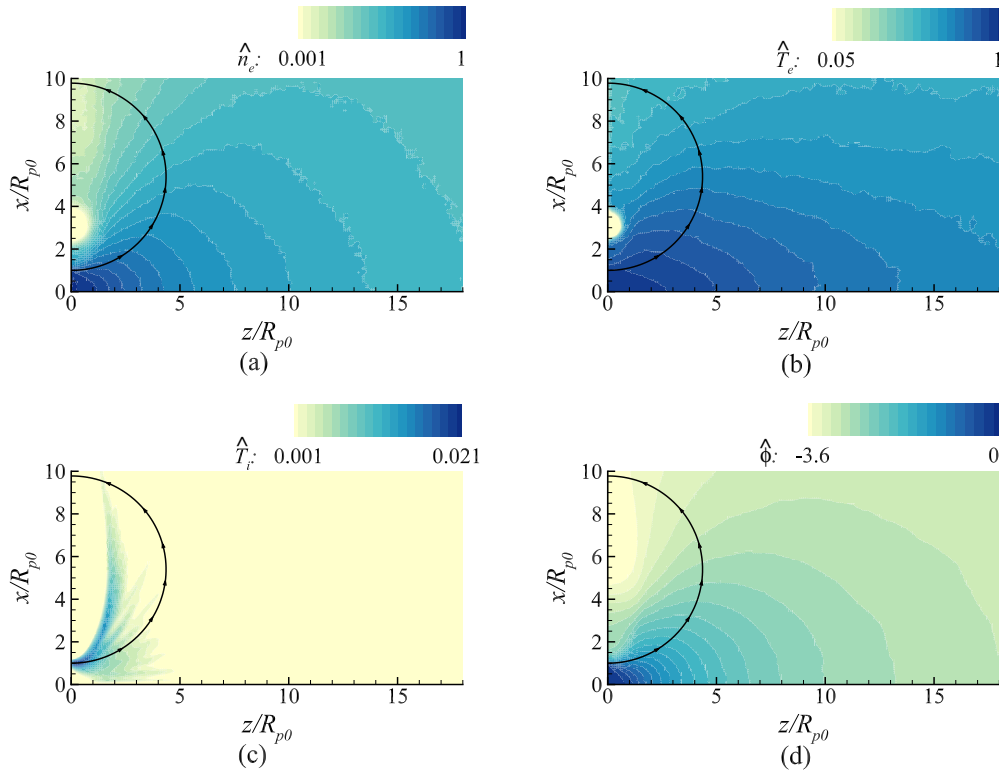


FIG. 5. Contour plots of normalized plasma parameters for simulation case  $T_{i0} = 0$ . (a) Electron density; (b) electron temperature; (c) ion temperature; (d) electric potential. The MDML is indicated by a bold black line with arrows.

as shown in Fig. 4(d). Although, in Fig. 4(e), the potential barrier drops slightly as the macroparticle number increases, the dropping tendency saturates quickly, and the curves nearly coincide with each other when the particle number is further increased from  $1.8 \times 10^6$  to  $2.2 \times 10^6$ . Therefore, the possibility of numerical diffusion has been excluded.

Figures 5 and 6 show the contours of the electron density, electron temperature, ion temperature, and electric potential under the condition of  $T_{i0} = 0$  and  $T_{i0} : T_{e0} = 2.4 : 1$ , respectively. It is worth noting that all the contour levels of number density and current density in this paper are in exponential scale, and that of other parameters are in linear scale, if not specified otherwise. And, some part of the domain (20 Debye lengths wide) near the open boundary has been omitted to avoid any error that could arise from the artificial boundary settings. The MDML, which is the projection of the magnetic flux surface that intersects  $(x, z) = (R_{p0}, 0)$  on the  $x$ - $z$  plane, is indicated by a bold black line with arrows on all the contours. As can be seen from Figs. 5 and 6 the electron density and potential distribution on the inner side of MDML are very similar to what has been published in the literature [33,38]. The ion temperature in Fig. 5(c) can be neglected compared to the electron temperature. The electron temperature and ion temperature distribution are shown in Figs. 6(b) and 6(c); note that temperatures of both species are normalized by  $T_{i0} + T_{e0}$ , thus the sum of the electron temperature and ion temperature at the plasma inlet approximates unity.

Comparing the contour plots of the electric potential in Figs. 5(d) and 6(d), when the ion temperature is considered, an obvious electric potential barrier centered approximately at  $\hat{z} = 1$  appears on the periphery of the magnetic nozzle

throat (i.e., the outer-MDML area) while it does not appear in Fig. 5(d), in which case  $T_{i0}$  is set to 0 eV.

This potential structure has a close relationship with the ion and electron confinement in the magnetic nozzle and is similar in nature with the side lobe discovered by Charles [41] and the potential well reported by Little and Choueiri [43]. In our simulation, the gyroradii of electrons and ions satisfy the following relationship:  $r_{L,e} \approx 0.16R_{p0} \ll R_{p0}$  and  $r_{L,i} \approx 12R_{p0} \gg R_{p0}$ , indicating ions are unmagnetized while electrons are strongly magnetized. In this case, the cross-field motion of electrons is severely limited by the magnetic field, while that of the ions is mostly not influenced. Therefore, when the thermalized plasma beam is injected into the MN, the electrons will mostly move following the magnetic lines. However, the thermalized ions with large lateral velocity components comparable to their axial ones will move laterally outward, crossing the magnetic lines. Consequently, some of the ions overshoot the MDML, resulting in local charge separation and an accumulation of positive space charges beyond MDML. Therefore, a negative electric field  $E_{\perp}$  is established and the electric potential will rise to bound the fled ions to the magnetized electrons. This is the reason why the high-potential area forms.

In order to obtain a clear understanding of the phenomenon, the phase-space scatter plot of ions from the region  $0.75 < \hat{z} < 1.25$  and the profile of electric potential along  $\hat{z} = 1$  are shown in Fig. 7. Note that the left part of the figure is mirrored from the right part which is the one actually simulated by our code. As the figure shows, plenty of ions locate between MDML and the peak of the potential barrier (between the solid vertical line and the dashed vertical line).

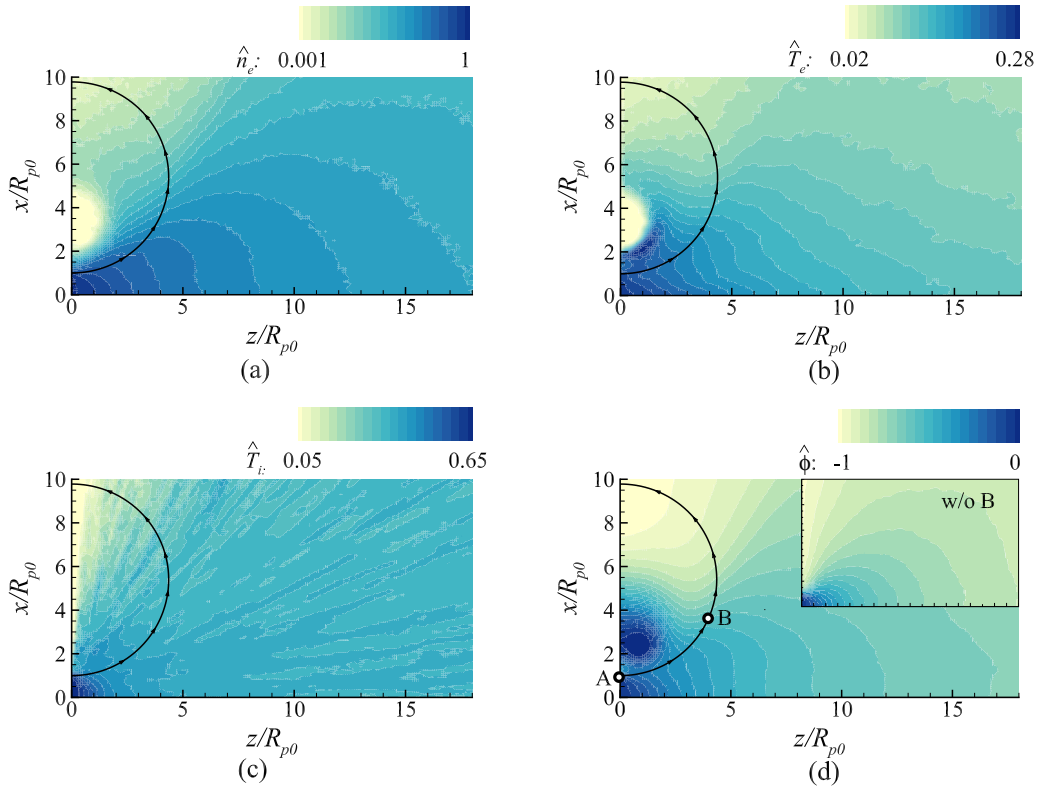


FIG. 6. Contour plots of normalized plasma parameters for simulation case  $T_{i0} : T_{e0} = 2.4 : 1$ . (a) electron density; (b) electron temperature; (c) ion temperature; (d) electric potential; additionally, the contour without magnetic field is shown in the upper right-hand corner. The MDML is indicated by a bold black line with arrows.

The closer to the peak of the potential barrier, the more ions locate near  $v_{ix}/v_{te0} = 0$ , some of which even cross to the other side of  $v_{ix}/v_{te0} = 0$ . In other words, many ions overshoot the MDML and are decelerated or even bounced back by the potential barrier, although a few ions with higher energy are scattered out of the beam. In addition, a vortex structure has formed in the phase plot of ions, which means the potential barrier may be accompanied by some plasma waves or instabilities as reported by Singh *et al.* [42].

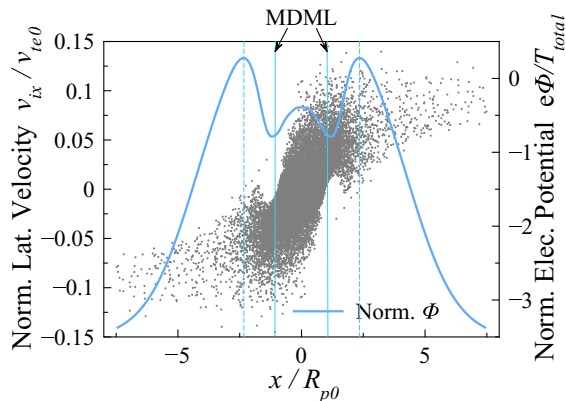


FIG. 7. Phase plot of ions from  $0.75 < \hat{z} < 1.25$  and the lateral profile of the electric potential along  $\hat{z} = 1$  in the  $T_{i0} : T_{e0} = 2.4 : 1$  case. The solid vertical line indicates the MDML, and the dashed vertical line denotes the position of the potential barrier peak.

However, it can be seen clearly from Fig. 6(d) that the extent of the potential barrier is not infinite and the electric potential descends both axially and laterally after reaching the peak. The reasons for this limited extent are threefold.

The first one is called finite-electron Larmor radius (FELR) effect as stated in the literature [65,66]. As shown in Fig. 6(d), point A locates at the edge of the plasma inlet, while point B is the intersection of the MDML and the vertical line  $\hat{z} = 4$ , where the potential barrier almost vanishes. In the  $T_{i0} : T_{e0} = 2.4 : 1$  case the gyroradii of electrons increases from  $0.15R_{p0}$  at point A to  $0.83R_{p0}$  at point B, which is comparable to the characteristic variation length of the magnetic field  $R_{p0}$ . Therefore, as the magnetic field decreases downstream, the electrons effectively demagnetize, compromising the charge separation which forms the electric potential barrier.

The second reason is named the short-circuiting effect. The magnetic nozzles with large divergence angle are often used due to the limited size of coil or magnet. Thanks to the continuous property of the magnetic line, the MDML will eventually wind back to form a complete loop and hence the electrons can flee along the curved magnetic lines and arrive at the downstream area in the  $x$  direction without direct motion in the  $B$ -perpendicular direction. Specifically, the current densities of ions and electrons on the  $x$ - $z$  plane of  $T_{i0} : T_{e0} = 2.4 : 1$  case are depicted in Fig. 8 to show the macroscopic flows of ion and electron currents. Note that the current densities are normalized by  $en_0v_{te0}$ . As is shown in Fig. 8, compared to the electrons, more ions overshoot into the outer-MDML area to form the potential barrier, while the more magnetized

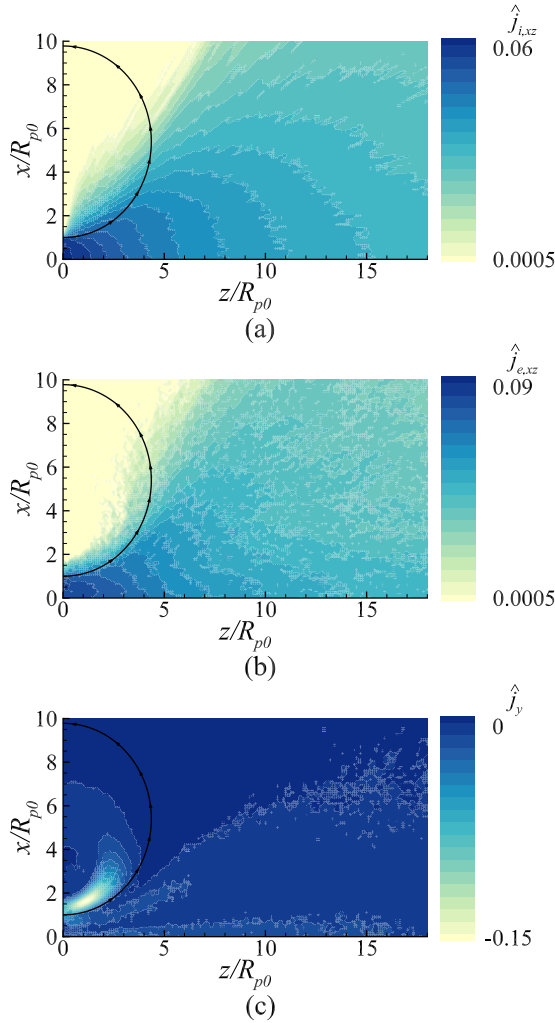


FIG. 8. Contours of normalized current density in the  $T_{i0} : T_{e0} = 2.4 : 1$  case. (a) Ion current density in the  $x$ - $z$  plane  $\hat{j}_{i,xz}$ . (b) Electron current density  $\hat{j}_{e,xz}$  in the  $x$ - $z$  plane. (c) Total current density in  $y$  direction  $\hat{j}_y$  (contour levels in linear scale).

electrons escape along the wind-back magnetic lines near MDML and neutralize the positive space charges which would otherwise accumulate along the descending part of the barrier. In other words, the electric potential barrier is short-circuited by the escaping electrons.

The third reason is the depletion of ion thermal energy. Comparing the distribution of  $\hat{\phi}$  in Figs. 5(d) and 6(d), when the ion thermal energy is canceled at the inlet, the potential barrier cannot form. In addition, the double-layer structure proposed as the driving force of the potential barrier by Rao and Singh [42,48] is not found under any of our simulation conditions. Therefore, the driving force of the barrier structure can be deduced as the ion thermal energy. According to Figs. 6(a) and 6(c), in the high- $T_{i0}$  scenario, the density and ion temperature drop fast near the inlet area, resulting in ions having insufficient thermal energy to expand and overshoot MDML in the downstream.

When turning off the magnetic field in the  $T_{i0} : T_{e0} = 2.4$  case, the obtained electric potential distribution is shown at the upper right-hand corner of Fig. 6(d). In this case, the

difference in magnetization between electrons and ions is eliminated, resulting in the lateral charge separation being compromised. The potential barrier vanishes, which confirms the role of magnetic field in the explanation above.

It can be concluded from the analysis above that both ion temperature and magnetic field are of significance for the formation of the electric potential barrier; therefore, a more quantitative investigation of these two factors is necessary.

## B. Influence of ion temperature and magnetic inductive strength

The same PIC model is used to conduct the investigation and four inlet temperature ratios are selected:  $T_{i0} : T_{e0} = 0, 0.8, 1.6, 2.4$  and the lateral potential distribution at  $\hat{z} = 1$  is shown in Fig. 9(a). Note that, to demonstrate the trend of the relative magnitude of the potential barrier, the ratio of local electric potential and the corresponding value at the symmetric plane  $\hat{\phi}/|\hat{\phi}_{\text{sym}}|$  is used rather than the original normalized potential  $\hat{\phi}$ . As can be seen from Fig. 9(a), the relative magnitude (defined as  $(\hat{\phi}_{\text{max}} - \hat{\phi}_{\text{min}})/|\hat{\phi}_{\text{sym}}|$ ) of the potential barrier increases from 0.56 to 2.67; as the temperature ratio increases from 0.8 to 2.4, more ions overshoot beyond the MDML. On the other hand, the thermal energy of the electrons is lowered, so are the electrons' Larmor radii, and then the FELR effect which undermines the charge separation is suppressed. In turn, larger electric field is generated to counter the local charge separation, resulting in an even higher potential barrier. As shown in Fig. 8(c), the lateral electric field along with lateral density gradient induces large diamagnetic currents outside of MDML; thus, the laterally outward electric force experienced by electrons is transferred to the coils through Lorentz force generated by these diamagnetic currents. The confinement effect of the potential barrier can be seen in Fig. 9(b), in which the lateral profile of ion number density  $\hat{n}/\hat{n}_{\text{sym}}$  (normalized with the corresponding value at the symmetric plane  $\hat{n}_{\text{sym}}$ ) and a vertical dashed line indicating the peak of the potential barrier are illustrated. When  $T_{i0} = 0$ , the ions only expand slightly; the number density of ions quickly vanishes at  $\hat{x} = 2$ , while the ions are still well constrained within the dashed line by the potential barrier as the temperature increases—the ion number density on the dashed line is less than 10% of that on the symmetric plane.

The magnetic inductive strength is another variable worth to be investigated. The value  $B_0$  at (0,0) is used as a reference. At a fixed inlet temperature ratio  $T_{i0} : T_{e0} = 2.4 : 1$ , the simulation was conducted under 7 magnetic inductive strengths covering 4 orders of magnitude:  $B_0 = 0, 0.02, 0.1, 0.2, 1, 2, 3$  T. The simulated lateral profiles of the relative potential are demonstrated in Fig. 9(c). Under the condition  $B_0 = 0.02$  T or below, the profile shows no sign of potential barrier because the gyroradius of electrons is  $1.6R_{p0} > R_{p0}$ , which is clearly unmagnetized. The lateral separation of charges is mostly compromised by the FELR effect. When  $B_0 \geq 0.1$  T, the potential barrier appears and its relative magnitude increases from 0.15 to 6.33 as  $B_0$  rises from 0.1 to 2 T and then decreases to 4.72 under  $B_0 = 3$  T, forming a unimodal profile shown in Fig. 9(d). The effect of magnetic inductive strength on the gyrocyclone frequency is  $\frac{d\omega_c}{dB} = \frac{e}{m_s}$ , where  $m_s$  means the mass of the particle species. Due to

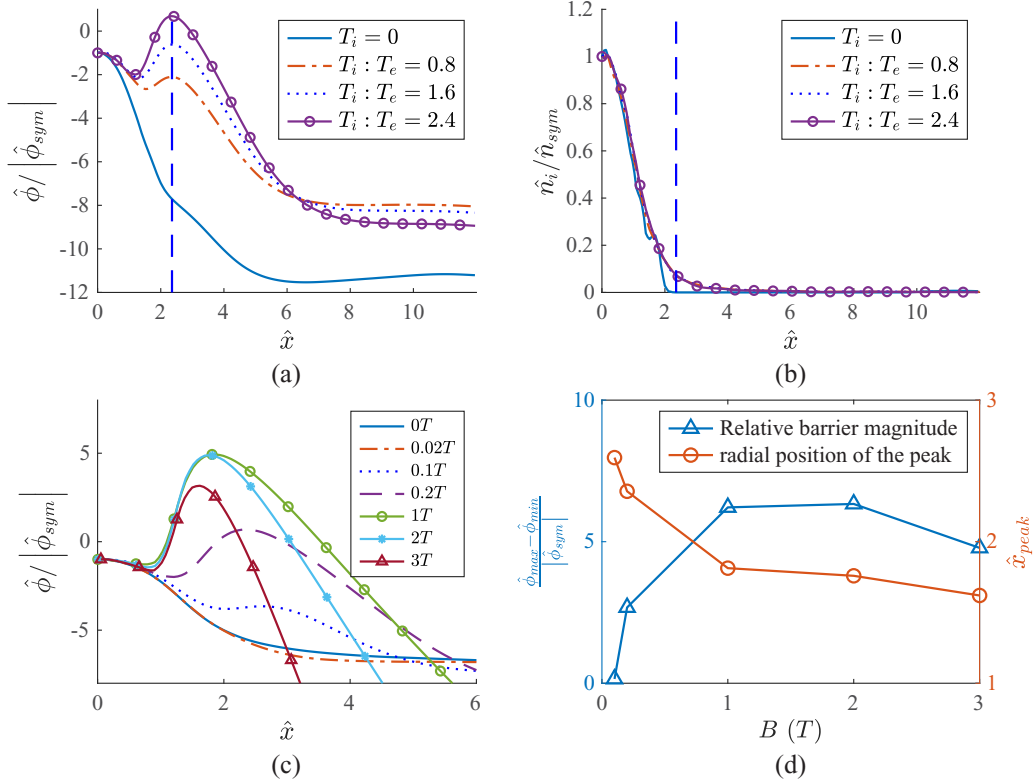


FIG. 9. Quantitative investigation of the potential barrier. (a) Relative potential vs lateral coordinate at  $\hat{z} = 1$  (under different  $T_{i0} : T_{e0}$ ); (b) relative ion number density vs lateral coordinate at  $\hat{z} = 1$  (under different  $T_{i0} : T_{e0}$ ); (c) relative potential vs lateral coordinate at  $\hat{z} = 1$  (under different  $B_0$ ); (d) relative magnitude and lateral position of potential barrier peak vs  $B_0$ .

the small mass of the electron,  $B_0$  has a greater influence on the magnetization degree of the electrons, while the ions are mostly unaffected in the low magnetic-field scenario. The electron Larmor radius decreases from infinite ( $B_0 = 0$ , unmagnetized) to a finite value; thus, the lateral movement of electrons is more and more suppressed when increasing  $B_0$ , while the ions can overshoot the MDML almost ballistically. Therefore, the charge separation across the MDML aggravates and a greater potential barrier forms to counteract this trend. This is another clear manifestation of the finite-electron Larmor radius effect in the MN. However, this positive correlation between the potential barrier and  $B_0$  cannot be extended to the high- $B_0$  scenario. As  $B_0$  continues to grow to 3 T, the electron Larmor radius decreases to  $0.01R_{p0} \ll R_{p0}$ , and the electrons approach the fully magnetized limit so that the lateral motion of electrons is no longer sensitive to  $B_0$ . On the contrary, the ion Larmor radius is  $0.79R_{p0}$ , which means the ions start to be magnetized to an extent so intense that the overshooting of ions is obviously restrained. The interesting indication here is that the charge separation is in turn hindered by the ever-increasing magnetic field, resulting in the drop of the potential barrier. At this situation, the ion Larmor radius becomes comparable to the characteristic length  $R_{p0}$ , and the magnitude variation is dominated by the magnetization degree of ions. This effect can be named accordingly as finite-ion Larmor radius (FILR) effect. Additionally, as can be seen from Fig. 9(d), the lateral position of the barrier moves closer to the symmetric plane as  $B_0$  increases, which is due to the greater deceleration effect caused by the higher potential

barrier; the average overshooting distance becomes shorter, resulting in better confinement in the magnetic nozzle.

The results of the quantitative investigation are consistent with the proposed mechanism of the potential barrier. The temperature ratio and the magnetic inductive strength represent two factors responsible for the behaviors of the potential barrier: (1) Ion thermal energy is the driving force of the ion overshooting and monotonically provokes the charge separation. (2) Magnetic field limits both the lateral motion of electrons and ion overshooting yet has a mixed influence on the charge separation depending on the magnetic inductive strength. In the study of the influence of  $B_0$ , the magnitude of electric potential barrier presents a unimodal profile, which essentially reflects the transfer of dominance in the plasma confinement of the magnetic nozzle, from the FELR effect in the lower magnetic-field scenario to the FILR effect in the higher one.

In either scenario, the potential barrier deflects or reflects ions with lower energy, but the ions in the high-energy tail of the Maxwellian distribution can still pass the potential barrier. From the number density profile in Fig. 9(b), most of the ions are trapped inside. From the perspective of momentum transfer, part of the nonaxial momentum of thermalized ions is consumed by the potential barrier and transferred to the magnetized electrons, which in turn transfer the momentum through Lorentz force to the coils, generating the thrust from ion thermal energy.

In order to analyze the contribution of ion thermal energy to the thrust under high- $T_{i0}$  scenario, a simulation case was

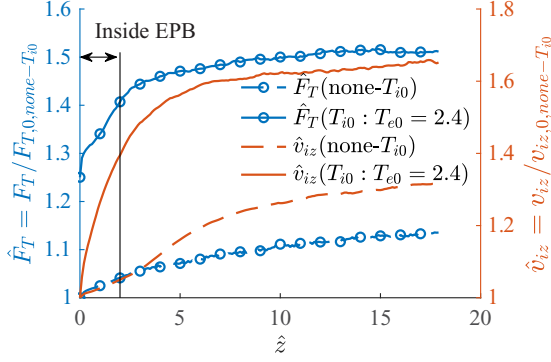


FIG. 10. Axial profile of normalized thrust  $\hat{F}_T$  and  $z$  component of ion velocity along the symmetric plane  $\hat{v}_{iz}$ .

conducted, in which the ion temperature at the inlet is set to 0 eV while retaining other parameters the same as in the  $T_{i0} : T_{e0} = 2.4$  case above. The simulated axial profiles of thrust and ion axial velocity along the symmetric plane in these two cases are compared in Fig. 10 below. In the figure, the thrust  $\hat{F}_T$  and velocity  $\hat{v}_{iz}$  are normalized by the corresponding value at the inlet of the none- $T_{i0}$  case to better show the relative contribution inside the MN. As can be seen from the figure, the none- $T_{i0}$  case obtained a maximum thrust augmentation  $\Delta\hat{F}_T = 0.14$  at the farthest downstream, while the largest one in the high- $T_{i0}$  case is 0.52, which means the ion thermal energy contributes 73.1% of the thrust augmentation. In terms of the ion axial velocity, the none- $T_{i0}$  case obtains a highest velocity increase  $\Delta\hat{v}_{iz} = 0.33$ , which is only 50% of  $\Delta\hat{v}_{iz} = 0.66$  in the high- $T_{i0}$  case. Therefore, the thrust and ion acceleration contributed by the ion thermal energy are considerable under the high- $T_{i0}$  scenario. As shown in Figs. 6(c) and 6(d), the electric potential barrier mainly extends from  $\hat{z} = 0$  to  $\hat{z} = 2$ , and the ion temperature drops rapidly in this area; at the same time, in Fig. 10 the velocity increase  $\Delta\hat{v}_{iz}$  of high- $T_{i0}$  case has completed 59.9% of the total value inside this area too. Thus, we can conclude that the magnetic nozzle surrounded by the electric potential barrier is the main place for ion acceleration in the high- $T_{i0}$  scenario.

From this perspective, the magnetic nozzle surrounded by the potential barrier is like a de Laval nozzle which transfers the nondirected energy of ions to the directed one. Specifically, the potential barrier acts like a “filterlike wall”—high-energy ions give up part of their energy and escape the constraint, but most of the ions are trapped by the electric potential barrier.

### C. Differences and connections between the electric potential barrier in MN and other similar phenomena

Similar electric potential structures have been observed in other numerical simulations [42,48] and experiments [41,65], thus the differences and connections between them and the electric potential barrier should be addressed.

The high potential observed in the simulation of Merino and Ahedo [38] is different from the electric potential barrier we discovered in nature. Firstly, the high potential they obtained in their results was located within the most divergent magnetic line (MDML), which is the direct downstream area

of the plasma inlet, whereas the electric potential barrier we discovered locates outside of the MDML. The simulation domain of Merino and Ahedo did not include the area outside of the MDML because of the limitation of their integration method, which is clearly stated in the appendix of Ref. [49]. Moreover, the nature of the electric potential barrier we investigated is charge separation and the accumulation of positive space charges outside MDML, while this is forbidden by the quasineutrality assumption of the fluid method employed by Merino and Ahedo.

Similar to the electric potential barrier presented here, Charles [41] and Little and Choueiri [43,65] also observed high potential structures in the plume of HPTs. Charles observed a high potential area which coincides with a conical density structure which does not appear in Little’s observation. The reason for this difference might be the crucial differences in the size and material of their vacuum facilities. The vacuum tank that Charles employed is a relatively small one with a grounded conducting wall, while the one used by Little and Choueiri is a large dielectric facility. This difference can be reflected in the boundary settings of the simulations. In our simulation, a Neumann boundary condition  $\partial\phi/\partial n = 0$  is set at the open boundary for the solution of electric potential, which approximates more closely to the dielectric wall. Rao and Singh also found a potential side lobe at the edge of the magnetic nozzle throat [42,48], whereas they used a conducting boundary condition  $\phi = 0$  for the open boundary which represents the grounded chamber in the experiment of Charles. In addition, the conical density structure that appeared in the experiments of Charles and the simulation results of Rao and Singh does not exist in our simulation results either. Therefore, the potential barrier from our simulation is more similar to the one observed by Little and Choueiri.

In the work of Rao and Singh, the cause of the sidelobe is the accumulated positive space charges resulted from the overshooting of ions which are accelerated laterally by the double layer. However, in this work, no double layer was observed in the results; the driving force behind the potential barrier is the initial thermal energy of ions, which is another factor affecting this kind of phenomenon.

In summary, despite the reports in the literature mentioned above, our work is original in the following aspects. Firstly, this work directly relates initial ion temperature to the electric potential barrier in the MN, which was found to be the driving force of the potential barrier with our simulation conditions. The influences of  $T_{i0} : T_{e0}$  are investigated, and its relation with the generation of gas dynamic thrust from the ion thermal energy is addressed. Secondly, the study of the effects of the magnetic inductive strength has been extended to the high- $B_0$  scenario, where the FILR effect is put forward and found to dominate the plasma confinement of the MN rather than the FELR effect. Thirdly, besides the FELR effect, two more reasons for the limited extent of the potential barrier are put forward—the depletion of ion thermal energy and the short-circuiting effect.

## V. CONCLUSIONS

In this paper, some overlooked physics in confining thermalized ions in magnetic nozzles are investigated by a fully

kinetic planar-3V PIC model, and a potential barrier is discovered on the periphery of the magnetic nozzle throat, which is responsible for the ion confinement. The lateral overshooting of thermalized ions results in an accumulation of positive space charges beyond MDML, leading to this potential barrier whose extent is limited by the FELR effect, the depletion of ion thermal energy, and the short-circuiting effect. The quantitative investigation shows that the relative magnitude of potential barrier, defined as  $(\hat{\phi}_{\max} - \hat{\phi}_{\min})/|\hat{\phi}_{\text{sym}}|$ , increases from 0.56 to 2.67 as the inlet temperature ratio  $T_{i0} : T_{e0}$  rises from 0.8 to 2.4. Moreover, as the magnetic field strengthens from 0 to 3 T, the relative magnitude shows a unimodal profile with a peak value of 6.33 at  $B_0 = 2$  T and the potential barrier moves from  $\hat{x} = 2.59$  to  $\hat{x} = 0.62$ —closer to the symmetric plane. Lastly, the potential barrier serves as a medium that transfers the ion pressure to the magnetic nozzle, resembling a solid wall in a de Laval nozzle. In the  $T_{i0} : T_{e0} = 2.4 : 1$  case, the contribution of ion thermal energy covers 73.1% of the thrust augmentation and the magnetic nozzle surrounded by the potential barrier is found to be the main place for ion acceleration. The study of the electric potential barrier provides a deeper insight into the physics behind the ion confinement and thrust generation mechanism of magnetic nozzles and serves as guidance in designing magnetic nozzles for plasma propulsion systems or other similar applications. However, the nature of the latent plasma waves or instabilities accompanying the potential barrier, the influence on the particle acceleration, and detachment processes still require detailed investigations, which will be addressed in the future work.

#### ACKNOWLEDGMENTS

This work was supported by the National Natural Science Foundation of China (Grant No. 11872093). The authors would like to thank Prof. Joseph. J. Wang from University of Southern California for the useful talks about this work. The authors also want to thank Prof. Eduardo Ahedo and Associate Prof. Mario Merino from University Carlos III of Madrid for their guidance and inspirations during the development of the code. It is also a pleasure to thank Dr. Zun Zhang for her professional knowledge on the double layer and Yifeng Fu for the discussion on plasma instabilities.

#### APPENDIX: DERIVATION PROCESS OF THE PLANAR-TO-CYLINDRICAL SCALING LAWS FOR THE NUMBER DENSITY AND ELECTRIC POTENTIAL ALONG THE AXIS

Assume a magnetic flux tube along the magnetic nozzle axis that is separated into many disks along the  $z$  direction with equal interval  $\Delta L$ . In the paraxial limit, the magnetic inductive strength on the cross section of the tube is assumed uniform and can be represented by  $B(z)$  on the axis. Since the magnetic flux is conserved in the tube, the cross-sectional area  $A(z)$  varies with  $B(z)$ ,

$$A(z) = \frac{B_0}{B(z)} A_0. \quad (\text{A1})$$

Thus, the radius of the magnetic flux tube  $R(z)$  also varies with  $B(z)$  as

$$R(z) = \sqrt{\frac{B_0}{B(z)}} R_0, \quad (\text{A2})$$

where the subscript 0 represents the quantity at  $z = 0$ .

Now we can derive the plasma number density under both the planar and cylindrical geometries. In the cylindrical geometry, each disk mentioned above is a cell and the magnetic flux tube is a one-dimensional grid. However, in the planar geometry, the volume of the cell is changed into a slat whose size is  $2R(z) \times \Delta L \times \Delta L$  in the  $x, y, z$  direction, which means the cell size in the  $y$  direction is also  $\Delta L$ . Despite different geometries, the number of electrons in each cell  $N(z)$  is supposed to be the same, and then the scaling law of number densities in different geometries can be derived. Note that the normalization in length has been made by  $\Delta L$ .

The expression for cross-sectional area in the planar geometry is

$$A_{\text{planar}}(z) = 2R(z)\Delta L = 2\hat{R}(z)(\Delta L)^2, \quad (\text{A3})$$

while the cross-sectional area in the cylindrical geometry is

$$A_{\text{cyl}}(z) = \pi R(z)^2 = \pi \hat{R}(z)^2 (\Delta L)^2 \quad (\text{A4})$$

The number densities in the two geometries are

$$n_{\text{planar}}(z) = \frac{N(z)}{A_{\text{planar}} \Delta L}, \quad (\text{A5})$$

$$n_{\text{cyl}}(z) = \frac{N(z)}{A_{\text{cyl}} \Delta L}, \quad (\text{A6})$$

From Eq. (A5) and Eq. (A6), we have

$$\frac{n_{\text{cyl}}(z)}{n_{\text{planar}}(z)} = \frac{A_{\text{planar}}(z)}{A_{\text{cyl}}(z)} = \frac{2}{\pi \hat{R}(z)}, \quad (\text{A7})$$

$$n_{\text{cyl}}(z) = n_{\text{planar}}(z) \frac{2}{\pi \hat{R}(z)}, \quad (\text{A8})$$

$$n_{\text{cyl}0} = n_{\text{planar}0} \frac{2}{\pi \hat{R}_0}. \quad (\text{A9})$$

Dividing Eq. (A8) with Eq. (A9), we have

$$\hat{n}_{\text{cyl}}(z) = \hat{n}_{\text{planar}}(z) \frac{\hat{R}_0}{\hat{R}(z)}. \quad (\text{A10})$$

Substitute Eq. (A2) into Eq. (A10), and the scaling law to transfer planar number densities into their equivalents in the cylindrical geometry is obtained,

$$\hat{n}_{\text{cyl}}(z) = \hat{n}_{\text{planar}}(z) \sqrt{\frac{B(z)}{B_0}}. \quad (\text{A11})$$

Equation (6) is obtained by changing the subscript of  $\hat{n}_{\text{cyl}}(z)$  into ‘‘scaled’’ in Eq. (A11).

As for the electric potential, the Boltzmann relation is assumed along the axis. The electric potential and number density are normalized by  $\frac{k_B T_{e0}}{e}$  and  $n_0$  at the origin; thus, the relation between the normalized electric potential and number density is

$$\hat{\phi}(z) = \ln \hat{n}(z). \quad (\text{A12})$$

Therefore, in both geometries,

$$\hat{\phi}_{\text{planar}}(z) = \ln \hat{n}_{\text{planar}}(z), \quad (\text{A13})$$

$$\hat{\phi}_{\text{cyl}}(z) = \ln \hat{n}_{\text{cyl}}(z). \quad (\text{A14})$$

Subtracting Eq. (A13) from Eq. (A14), we have

$$\hat{\phi}_{\text{cyl}}(z) = \hat{\phi}_{\text{planar}}(z) + \ln \frac{\hat{n}_{\text{cyl}}(z)}{\hat{n}_{\text{planar}}(z)}. \quad (\text{A15})$$

Substitute Eq. (A11) into Eq. (A15), and the scaling law for the electric potential is obtained,

$$\hat{\phi}_{\text{cyl}}(z) = \hat{\phi}_{\text{planar}}(z) + \frac{1}{2} \ln \frac{B(z)}{B_0}. \quad (\text{A16})$$

Equation (7) is obtained by changing the subscript of  $\hat{n}_{\text{cyl}}(z)$  into “scaled” in Eq. (A16).

- 
- [1] K. Takahashi, *Rev. Mod. Plasma Phys.* **3**, 3 (2019).
- [2] Y. Arakawa and A. Sasoh, *J. Propul. Power* **8**, 98 (1992).
- [3] C. Charles and R. Boswell, *Appl. Phys. Lett.* **82**, 1356 (2003).
- [4] A. V. Arefiev and B. N. Breizman, *Phys. Plasmas* **11**, 2942 (2004).
- [5] M. Keidar, in *Proceedings of the 53rd AIAA Aerospace Sciences Meeting* (AIAA, Reston, VA, 2015).
- [6] K. F. Schoenberg, R. A. Gerwin, R. W. Moses Jr, J. T. Scheuer, and H. P. Wagner, *Phys. Plasmas* **5**, 2090 (1998).
- [7] C. Charles, R. W. Boswell, W. Cox, R. Laine, and P. MacLellan, *Appl. Phys. Lett.* **93**, 201501 (2008).
- [8] M. Merino and E. Ahedo, *Plasma Sources Sci. Technol.* **26**, 095001 (2017).
- [9] B. Lin and J. P. Sheehan, in *Proceedings of the 2018 AIAA Aerospace Sciences Meeting* (AIAA, Reston, VA, 2018), p. 0003.
- [10] S. A. Andersen, *Phys. Fluids* **12**, 557 (1969).
- [11] K. Kuriki and O. Okada, *Phys. Fluids* **13**, 2262 (1970).
- [12] I. Masaaki, A. Akira, H. Kunihiko, T. Hiroyuki, and Y. Tsuyoshi, *J. Plasma Fusion Res.* **78**, 1352 (2002).
- [13] K. Takahashi and A. Ando, *Phys. Rev. Lett.* **118**, 225002 (2017).
- [14] J. M. Little and E. Y. Choueiri, *Phys. Rev. Lett.* **117**, 225003 (2016).
- [15] K. Takahashi, C. Charles, R. Boswell, and A. Ando, *Phys. Rev. Lett.* **120**, 045001 (2018).
- [16] K. Takahashi, T. Lafleur, C. Charles, P. Alexander, and R. W. Boswell, *Phys. Rev. Lett.* **107**, 235001 (2011).
- [17] K. Takahashi, C. Charles, and R. W. Boswell, *Phys. Rev. Lett.* **110**, 195003 (2013).
- [18] B. Wang, H. Tang, Y. Wang, C. Lu, C. Zhou, Y. Dong, G. Wang, Y. Cong, D. Luu, and J. Cao, *J. Vis. Exp.* e58510 (2018).
- [19] G. R. Seikel and E. L. Walker, *Axisymmetric Expansion of a Plasma in a Magnetic Nozzle Including Thermal Conduction* (National Aeronautics and Space Administration, Washington, D.C., 1971).
- [20] D. L. Chubb, *AIAA J.* **10**, 113 (1972).
- [21] P. G. Mikellides, P. J. Turchi, and N. F. Roderick, *J. Propuls. Power* **16**, 887 (2000).
- [22] M. Li, H. Tang, J. Ren, and T. M. York, *Phys. Plasmas* **20**, 103502 (2013).
- [23] J. Cheng, H. Tang, and T. M. York, *Phys. Plasmas* **21**, 063501 (2014).
- [24] A. Fruchtman, *Phys. Rev. Lett.* **96**, 065002 (2006).
- [25] A. V. Arefiev and B. N. Breizman, *Phys. Plasmas* **15**, 042109 (2008).
- [26] J. P. Sheehan, B. W. Longmier, E. A. Bering, C. S. Olsen, J. P. Squire, M. G. Ballenger, M. D. Carter, L. D. Cassady, F. R. Chang Díaz, T. W. Glover, and A. V. Ilin, *Plasma Sources Sci. Technol.* **23**, 045014 (2014).
- [27] R. W. Moses, R. A. Gerwin, and K. F. Schoenberg, in *Proceedings of the Ninth Symposium on Space Nuclear Power Systems*, AIP Conf. Proc. No. 246 (AIP, New York, 1992), p. 1293.
- [28] E. B. Hooper, *J. Propuls. Power* **9**, 757 (1993).
- [29] A. V. Arefiev and B. N. Breizman, *Phys. Plasmas* **12**, 043504 (2005).
- [30] D. Kaufman, D. Goodwin, and J. Sercel, in *Proceedings of the 31st Aerospace Sciences Meeting* (AIAA, Reston, VA, 1993), p. 817.
- [31] J. M. Little and E. Y. Choueiri, in *Proceedings of the 47th Joint Propulsion Conference* (AIAA, Reston, VA, 2011).
- [32] E. Ahedo and M. Merino, *Phys. Plasmas* **18**, 053504 (2011).
- [33] A. V. Ilin, F. R. Chang-Diaz, J. P. Squire, A. G. Tarditi, B. N. Breizman, and M. D. Carter, in *Proceedings of the 40th AIAA Aerospace Sciences Meeting & Exhibit* (AIAA, Reston, VA, 2002).
- [34] R. Winglee, T. Ziemba, L. Giersch, J. Prager, J. Carscadden, and B. R. Roberson, *Phys. Plasmas* **14**, 063501 (2007).
- [35] M. Merino and E. Ahedo, *Plasma Sources Sci. Technol.* **25**, 045012 (2016).
- [36] M. Merino and E. Ahedo, in *Proceedings of the 47th Joint Propulsion Conference, San Diego, CA* (AIAA, Reston, VA, 2011).
- [37] S. A. Cohen and M. A. Paluszek, *Launchspace* **3**, 46 (1998).
- [38] M. Merino and E. Ahedo, *IEEE Trans. Plasma Sci.* **43**, 244 (2015).
- [39] M. Shoucri, E. Pohn, G. Knorr, P. Bertrand, G. Kamelander, G. Manfredi, and A. Ghizzo, *Phys. Plasmas* **7**, 2517 (2000).
- [40] M. Shoucri, H. Gerhauser, and K.-H. Finken, *Comput. Phys. Commun.* **164**, 138 (2004).
- [41] C. Charles, *Appl. Phys. Lett.* **96**, 051502 (2010).
- [42] N. Singh, S. Rao, and P. Ranganath, *Phys. Plasmas* **20**, 032111 (2013).
- [43] J. M. Little, *Performance Scaling of Magnetic Nozzles for Electric Propulsion* (Princeton University, Princeton, NJ, 2015).
- [44] M. Li, M. Merino, E. Ahedo, and H. Tang, *Plasma Sources Sci. Technol.* **28**, 034004 (2019).
- [45] S. Mahalingam, Y. Choi, J. Loverich, P. Stoltz, M. Jonell, and J. Menart, in *Proceedings of the 46th AIAA/ASME/SAE/ASEE Joint Propulsion Conference & Exhibit* (AIAA, Reston, VA, 2010), p. 6944.
- [46] S. Mahalingam, Y. Choi, J. Loverich, P. Stoltz, B. Bias, and J. Menart, in *Proceedings of the 47th AIAA/ASME/SAE/ASEE Joint Propulsion Conference & Exhibit* (AIAA, Reston, VA, 2011), p. 6071.
- [47] T. Yuan, J. Ren, J. Zhou, Z. Zhang, Y. Wang, and H. Tang, *AIP Adv.* **10**, 045115 (2020)..
- [48] S. Rao and N. Singh, *Phys. Plasmas* **19**, 093507 (2012).

- [49] E. Ahedo and M. Merino, *Phys. Plasmas* **17**, 073501 (2010).
- [50] J. P. Boris, in *Proceedings of the Fourth Conference on Numerical Simulation of Plasmas* (Naval Research Laboratory, Washington, D.C., 1970), pp. 3–67.
- [51] J. W. Eastwood and R. W. Hockney, *Computer Simulation Using Particles* (McGraw-Hill, New York, 1981).
- [52] K. L. Cartwright, J. P. Verboncoeur, and C. K. Birdsall, *J. Comput. Phys.* **162**, 483 (2000).
- [53] M. Li, M. Merino, E. Ahedo, J. Ren, and H. Tang, in *35th International Electric Propulsion Conference* (Georgia Institute of Technology, Atlanta, Georgia, 2017).
- [54] J. Wang, O. Chang, and Y. Cao, *IEEE Trans. Plasma Sci.* **40**, 230 (2012).
- [55] Y. Hu and J. Wang, *IEEE Trans. Plasma Sci.* **43**, 2832 (2015).
- [56] M. Merino, J. Mauriño, and E. Ahedo, *Plasma Sources Sci. Technol.* **27**, 035013 (2018).
- [57] Y. Jiang, H. Tang, J. Ren, M. Li, and J. Cao, *J. Phys. D: Appl. Phys.* **51**, 035201 (2018).
- [58] S. Cao, J. Ren, H. Tang, Z. Zhang, Y. Wang, J. Cao, and Z. Chen, *Phys. Plasmas* **25**, 103512 (2018).
- [59] H. Tang, J. Cheng, C. Liu, and T. M. York, *Phys. Plasmas* **19**, 073108 (2012).
- [60] H. Tang, J. Cheng, C. Liu, and T. M. York, *Phys. Plasmas* **19**, 073107 (2012).
- [61] O. V. Batishchev, *IEEE Trans. Plasma Sci.* **37**, 1563 (2009).
- [62] A. Negrotti, *Prog. Astronaut. Aeronaut.* **223**, 333 (2008).
- [63] K. Takahashi, D. Sato, K. Takaki, and A. Ando, *Plasma Sources Sci. Technol.* **22**, 055002 (2013).
- [64] K. Takahashi, A. Komuro, and A. Ando, *Phys. Plasmas* **23**, 033505 (2016).
- [65] J. M. Little and E. Y. Choueiri, *Phys. Rev. Lett.* **123**, 145001 (2019).
- [66] E. Ahedo and M. Merino, *Phys. Plasmas* **19**, 083501 (2012).